We are IntechOpen, the world's leading publisher of Open Access books Built by scientists, for scientists

4,800
Open access books available

122,000
International authors and editors

135M
Downloads

Our authors are among the

154
Countries delivered to

TOP 1%
most cited scientists

12.2%
Contributors from top 500 universities

CLARIVATE ANALYTICS
BOOK CITATION INDEX
INDEXED

WEB OF SCIENCE™

Selection of our books indexed in the Book Citation Index
in Web of Science™ Core Collection (BKCI)

Interested in publishing with us?
Contact book.department@intechopen.com

Numbers displayed above are based on latest data collected.
For more information visit www.intechopen.com

Defect Engineered 2D Materials for Energy Applications

Sai Sunil Kumar Mallineni, Sriparna Bhattacharya,
Fengjiao Liu, Pooja Puneet, Apparao Rao,
Anurag Srivastava and Ramakrishna Podila

Additional information is available at the end of the chapter

Abstract

Two-dimensional (2D) materials display unique properties that could be useful for many applications ranging from electronics and optoelectronics to catalysis and energy storage. Entropically necessary defects are inevitably present in 2D materials in the form of vacancies and grain boundaries. Additional defects, such as dopants, may be intentionally introduced to tune the electronic structure of 2D materials. While defects are often perceived as performance limiters, the presence of defects and dopants in 2D materials results in new electronic states to endow unique functionalities that are otherwise not possible in the bulk. In this chapter, we review defect-induced phenomena in 2D materials with some examples demonstrating the relevance of defects in electronic and energy applications. In particular, we present how the (i) N-dopant configuration in graphene changes the electron-phonon interactions, (ii) zigzag defects and edges in graphene increase the quantum capacitance to improve energy density of graphene-based supercapacitors, and (iii) charged grain boundaries in exfoliated Bi_2Te_3 preferentially scatter low-energy electrons and holes to enhance the thermoelectric performance.

Keywords: Engineering defects, 2D materials, Quantum capacitance, Energy storage

1. Introduction

Two-dimensional (2D) materials have intrigued physicists and material scientists for many decades due to an abundance of unusual physical phenomena that result from the confinement of charge, heat, and entropy flow to a plane [1]. For example, the ingenious harness of quantum mechanical phenomena, particular to lower dimensionality in graphene, has resulted

in intriguing observations such as the quantum Hall effect at room temperatures, quantized optical transmittance, nonlocal hot carrier transport, and Klein tunneling [2, 3]. Despite such fundamental breakthroughs, the potential of 2D materials has not yet completely manifested into practical devices due to material limitations [1, 4]. For instance, the lack of a band gap resulted in serious limitations for using graphene in electronics [4]. Defects in material science and engineering are often perceived as performance limiters, but in the case of 2D materials, defect engineering could provide a way to overcome many roadblocks and forge new frontiers. In this regard, others and we have shown that defects in 2D materials (e.g., dopants, vacancies) can provide an excellent handle to control material properties [5–8]. Specifically, we have shown that defects such as vacancies and N dopants in graphene could be used to control the electron-electron and electron-phonon scattering pathways [8]. These results provided critical breakthroughs for improving the quantum capacitance of graphene and doping graphene without compromising its intrinsic characteristics [6]. Defects also play a vital role in improving the properties of the so-called "beyond graphene" 2D materials. Previously, we used spark plasma sintering (SPS) to introduce charged grain boundaries (GB) in 2D Bi_2Te_3 for improving its thermoelectric (TE) figure of merit and compatibility factor [5]. Similarly, it has been demonstrated that defect engineering in 2D materials could improve many qualities ranging from electronic levels, conductivity, magnetism, and optics to structural mobility of dislocations and catalytic activities [9, 10]. As discussed in this chapter, defect engineering in 2D materials leads to the discovery of potentially exotic properties, which can enable unprecedented technological applications. In particular, we present how dopants and defects in (i) graphene could be used for optical and electrochemical energy storage applications and (ii) 2D Bi_2Te_3 could be controlled for enhancing its thermoelectric efficiency.

2. Nitrogen dopants for tuning the electronic and optical properties of graphene

Graphene is an ideal platform for many optoelectronic devices due to its distinctive combination of high electron mobility (μ), optical transparency, and gate/dopant-tunable carrier density [2]. However, to truly harness the potential of this combination and make graphene-based efficient optoelectronic devices a reality, optical and electronic properties of graphene must be tuned via substitutional doping [8]. While doping graphene with boron (B) or nitrogen (N) can tune the Fermi energy (E_F) and lead to p- or n-type graphene, it also compromises the inherently high electron mobility in doped graphene, which is useful for electronic applications [11–13]. Furthermore, the recombination rate of photogenerated carriers is also known to decrease with the presence of defects and dopants limiting applications of graphene in optoelectronics [8]. Indeed, the focus of many synthesis efforts in graphene has been to achieve large-area "defect-free" graphene for electronic applications because carrier-defect scattering limits the electron mobility—an important parameter for high-speed electronics [14–17]. Contrary to this conventional wisdom, we recently demonstrated that the defect configuration (in particular, N-dopant configuration in bilayer graphene lattice shown in **Figure 1a**) is more

important than the defect concentration for increasing carrier concentration without compromising photogenerated carrier lifetime [8].
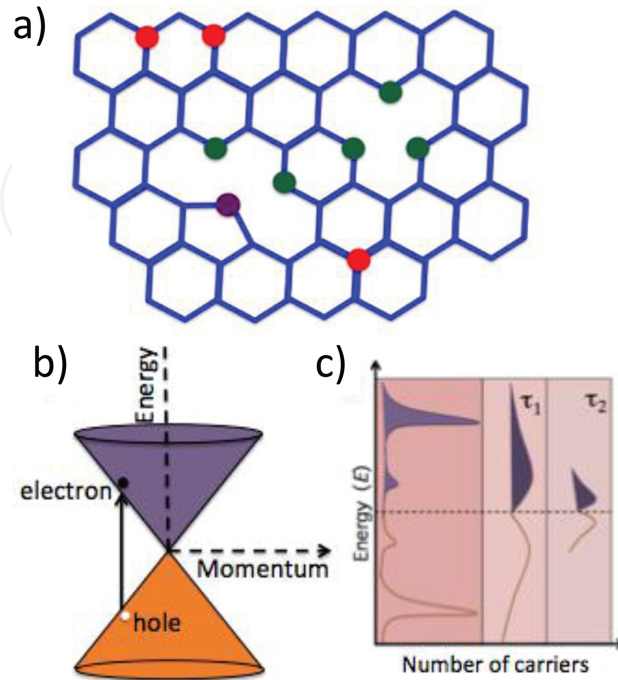
Figure 1. (a) Possible nitrogen dopant configurations in graphene lattice include pyridinic (green), pyrrolic (purple), and graphitic (red). While graphitic dopants (red) are purely substitutional, non-graphitic dopants (pyridinic and pyrrolic) result in additional defects such as vacancies or pentagons. (b) A schematic representation showing the linear energy dispersion for single-layer graphene and the arrow indicates excitation of electrons from the valence to the conduction band. (c) Under intense photoexcitation, the nonequilibrium carrier distribution (in the E-k space depicted by the energy dispersion shown in (b)) results in an initial rise in the transmitted intensity. The carriers (electron and hole distribution shown in blue and orange, respectively) equilibrate by carrier-carrier scattering on a timescale τ_1. Subsequently, the carrier thermalization and decay occur through carrier-phonon scattering on a timescale τ_2.

The electronic and optical properties of a single-layer graphene (SLG) can be described in terms of massless Dirac fermions with linear dispersion near the Fermi energy (**Figure 1b**). The semimetallic nature and electronic band structure of SLG allow for the photogeneration of electron-hole pairs at any wavelength in the visible-light spectrum [3]. This property is critical for many wide-bandwidth optoelectronic applications. As shown in **Figure 1b**, incident light excites electrons from the valence band (orange) into the conduction band (purple). Shortly after photoexcitation, incident photon-electron interactions create an out-of-equilibrium electron distribution (purple in **Figure 1c**), which initially relaxes on an ultrafast timescale ($\tau_1 \sim$ 100–300 fs) to a hot Fermi-Dirac distribution and subsequently cools via phonon emission or defect scattering ($\tau_2 \sim$ 1–2 ps) in graphene [8, 18]. In optoelectronic devices, when photoexcited electrons are scattered by phonons or defects, energy transferred to the lattice is dissipated as heat decreasing the net energy transported through charge carriers to drive a circuit. In the current scenario of graphene optoelectronic devices, a critical challenge is to increase the net charge carrier density and quench electron-defect relaxation pathways to extend photogenerated carrier lifetime.

The influence of defects on photogenerated carriers could be accounted by the inclusion of an extra term (A) in the expression for carrier scattering rate τ^{-1} (N) = A + BN + CN^2, where A represents nonradiative recombination, usually due to defects or traps, B represents radiative recombination, N is the carrier density, and C represents Auger recombination. The photo-generated carriers are quickly cooled to ground state through scattering by defects (represented by A) in addition to the existing carrier-carrier and carrier-phonon scattering (term B) and Auger recombination (term C). In the context of optoelectronic applications, it is imperative to identify ideal dopant concentration and configuration in graphene for which A in the carrier scattering rate equation is minimized. As mentioned earlier, heteroatomic doping can tune E_F and alter density of states (DOS) and thereby modify its electronic and optical properties. For instance, N-doping in chemical vapor deposition (CVD) graphene resulted in a bandgap due to the suppression of electronic density of states near the Fermi level and a consequent reduction in μ [19, 20]. As mentioned earlier, it is well known that N atoms can be substitutionally doped in the graphene lattice either in the pyridinic, pyrrolic, or graphitic configurations (see **Figure 1a**). Our density functional theory (DFT) calculations previously showed that all the three dopant configurations (viz., pyridinic, pyrrolic, and graphitic) are stable structures with a positive energy (>9.5 eV) released during the formation with graphitic dopants exhibiting the highest stability (**Figure 2**) [8].
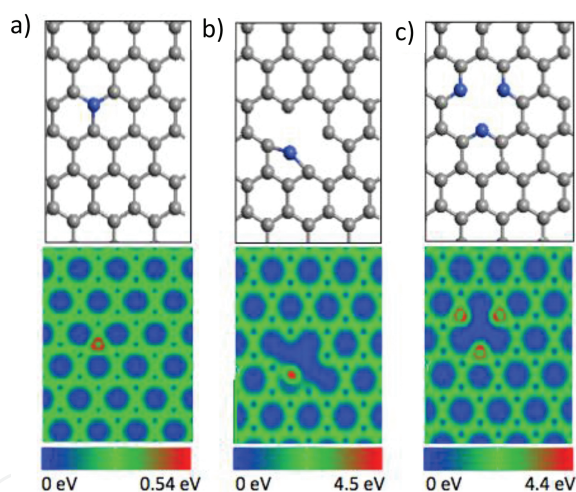
Figure 2. The lattice structure (top three panels) of graphitic (a), pyridinic (b), and pyrrolic (c) defects in graphene along with their electron density, obtained from our DFT calculations, shown in the bottom panels. The energy released on the formation of structure from free atoms for all the configurations was found to be positive (graphitic, 10.22 eV; pyridinic, 9.77 eV; and pyrrolic, 9.55 eV) confirming the stability of N-doped configurations.

2.1. CVD synthesis of N-graphene

Previously, we employed atmospheric pressure chemical vapor deposition (CVD) method for growing N-graphene [7]. This CVD set up consisted of a Cu foil loaded inside a 1 in. quartz tube at a temperature of 1,000 °C. Methane gas was used as the carbon source for graphene growth, while acetonitrile (AN) and benzylamine (BA) were used as precursors for N dopants in varying concentrations. The reaction was carried out under inert atmosphere by passing a

mixture of Ar and H_2 through the quartz tube reaction chamber. In particular, 450 sccm of Ar and 50 sccm of H_2 were used, and 2 sccm of methane was bubbled through the mixture of BA and AN. The volume percent of BA and AN varied in the ratio of 0:1, 1:1, and 3:1. Accordingly, the obtained samples were labeled S1, S2, and S3, respectively. Interestingly, we found that the N-dopant configuration (viz., graphitic, pyrrolic, and pyridinic) could be controlled using the ratio of BA to AN precursors.

2.2. The effects of N dopants in graphene: X-ray and Raman spectroscopy

We observed a strong correlation between the N-dopant configuration and the accompanying vibrational properties of N-doped CVD graphene: the N atoms bonded in the non-graphitic configurations (pyridinic and pyrrolic, observed using X-ray photoelectron spectroscopy or XPS) resulted in intense Raman disorder bands unlike the N atoms bonded in the graphitic configuration, even though the concentration of N dopants was higher in the latter case [7].

As shown in **Figure 3a**, we identified XPS peaks corresponding to graphitic, pyrrolic, and pyridinic configurations [21]. For pyridinic configuration, the N1s peak positions reported in the literature are usually in the range 398.1–399.3 eV. Similarly, pyrrolic configuration gives rise to peaks in the range 399.8–401.2 eV, while the peak around 400.5 eV (blue colored) is associated with the graphitic configuration. The orange-colored peak at ~401.5 and 406 eV may be attributed to different nitrogenated adsorbents [20, 21]. XPS results confirmed that the atomic percentages of nitrogen in S1, S2, and S3 were 0.2, 2.5, and 3.8 %, respectively [7]. It is important to note that S1 and S3 showed more non-graphitic N dopants compared to S2, which was purely graphitic doping. In order to further understand the effect of various nitrogen-doping configurations and concentrations on the electronic structure of graphene, we performed Raman spectroscopy of the samples S1, S2, and S3. The Raman spectrum of graphene displays four important bands [22, 23]: (i) the disorder or D band appears ~1350 cm^{-1} due to the presence of defects such as edges, grain boundaries, or any other type of defects including dopants in the graphene lattice; (ii) in some studies, researchers have also reported the presence of D′-band ~1600–1625 cm^{-1} in the Raman spectrum of highly disordered graphene [22]; (iii) the graphitic G band ~ 1585 cm^{-1} arises due to doubly degenerate optical phonon modes at the Brillouin zone center. It is a first-order Raman scattering process, and (iv) the 2D band ~ 2700 cm^{-1} is a consequence of second-order Raman scattering process involving intervalley scattering of in-plane transverse optical (*iTO*) phonons. Unlike the D band, which requires the presence of a defect to conserve the momentum of scattered electron along with an *iTO* phonon, 2D band does not require the presence of any defect due to the involvement of two *iTO* phonons and is always present in Raman spectra of both pristine and doped graphene [22]. The shape and width of the 2D band are sensitive to the number of layers in graphene. For example, 2D band in single-layer graphene (SLG) can be fit into a single Lorentzian peak, while for bilayer graphene, 2D band can be deconvoluted into four sub-peaks [23].

As seen in **Figure 3b**, the Raman spectra of pristine graphene samples did not exhibit strong D band in our studies. While samples S1 and S3, which contain non-graphitic doping configuration of nitrogen, showed strong D bands, the D band in sample S2 (graphitic) is similar to

that in pristine sample despite higher dopant concentration (~2.5 %). These results are consistent with our observations in the XPS spectra shown in **Figure 3a**. When nitrogen atoms enter the graphene lattice in non-graphic configuration, vacancies are needed and result in armchair-type edges. Previous reports showed that armchair edges in graphene allow intervalley scattering of *iTO* phonons in the Brillouin zone unlike zigzag edges [22] and thus increase the intensity of the D band as in samples S1 and S3.
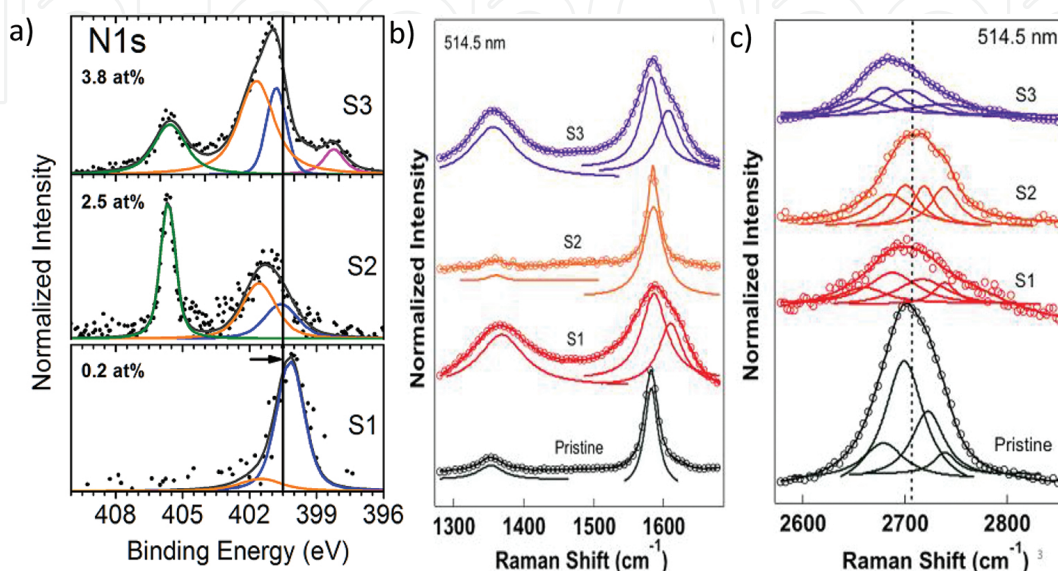

Figure 3. (a) XPS spectra for N1s line. The colored peaks represent the deconvolution of N1s peaks. The resolution of the spectrometer was 0.5 eV. The peak at 400.5 eV corresponds to graphitic configuration. Peaks at 398 and 400 eV correspond to non-graphitic. Raman spectra of pristine and N-graphene are shown in (b) and (c). As seen in (b), the D and D′ bands increase in intensity for non-graphitic samples S1 and S3. The deconvolution of 2D band in (c) suggests that graphene samples are bilayer.

From the line-shape analysis of Raman 2D band (**Figure 3c**), we confirmed that our CVD-grown graphene samples are predominantly bilayers. As seen in **Figure 3c**, maximum downshift in 2D band (25 cm^{-1}) was observed for sample S3 with relatively large dopant percentage (~3.5 %). On the other hand, sample S2 (graphitic configuration) showed little downshift in 2D band compared to sample S1 in spite of having higher dopant concentration. 2D band in S1 showed a downshift of ~10–15 cm^{-1} even in the presence of low dopant concentrations (~0.2 %). These differences in the 2D band shift in the Raman spectra can also be attributed to the nature of the dopant environment. For example, in samples S1 and S3 that are non-graphitic in nature, due to lattice symmetry breaking, electronic structure of graphene is strongly perturbed leading to possible renormalization of electron and phonon energies. Such a renormalization in electron energies results in a concomitant downshift in phonon energies of 2D band [7].

2.3. Nonlinear optical studies of N-graphene

We further explored the influence of defects on the carrier scattering rate using pump-probe (PP) spectroscopy [8]. The differential transmittance ($\Delta T/T$) was obtained by taking the ratio of pump-induced change in the probe transmittance (ΔT) at a time t after the pump excitation

to the probe transmittance (T) in the absence of a pump (**Figure 4a**). The initial response is an incident pulse-width-limited rise in the transmitted signal immediately after the zero delay ($t = 0$), which eventually decays in an exponential manner. The best fit to the PP data was obtained with a bi-exponentially decaying function, $\Delta T/T = A_1 \exp(-t/\tau_1) + A_2 \exp(-t/\tau_2)$ with two distinct time scales: a fast component (τ_1) corresponding to the intraband carrier-carrier scattering and a slower component (τ_2) corresponding to carrier-phonon scattering (discussed before in **Figure 1b**). Both τ_1 and τ_2 values obtained from the best-fitted curves for the samples are tabulated in **Figure 4b**. As shown in **Figure 4b**, the carrier-carrier and carrier-phonon relaxation times do not decrease monotonically with increasing N content, akin to the Raman features described in **Figure 3**. Clearly, the dopants present in the non-graphitic configurations exhibit much faster relaxation times relative to dopants present in S2 with graphitic bonding or pristine graphene. Indeed, carriers in sample S1 decay much faster (within fs), despite lower N content, due to the presence of extended defects that lead to increased contribution from carrier-defect scattering. More importantly, N dopants in graphitic configuration do not affect the carrier recombination times even at >1 % doping, while pyrrolic/pyridinic configurations drastically decrease carrier lifetimes at concentrations as low as ~0.2 %.

| Sample ID	τ_1	τ_2
Pristine	241 fs	
S1	196 fs	206 fs
S2	232 fs	1.6 fs
S3	168 fs	186 fs
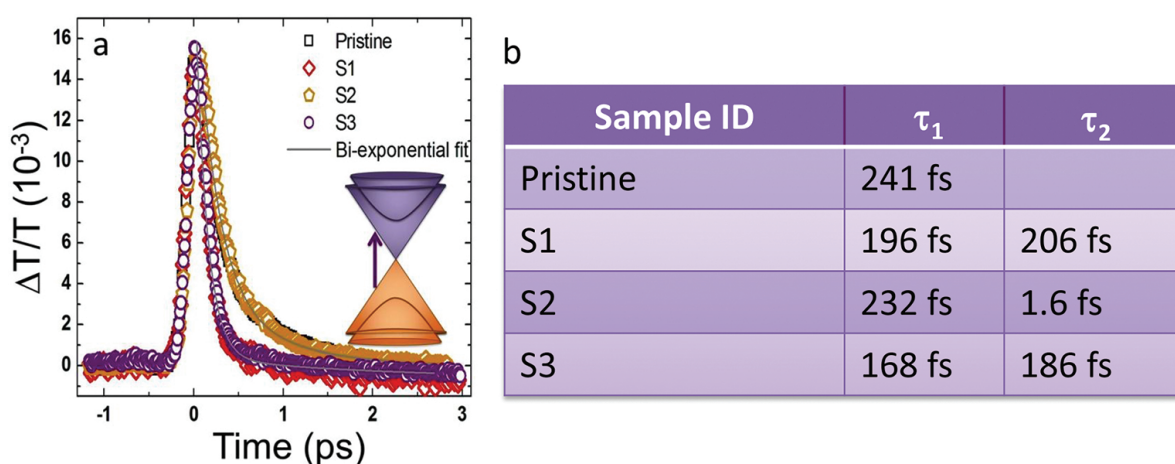
Figure 4. (a) Time-resolved differential transmission spectra of pristine and N-doped graphene samples S1, S2, and S3, respectively, obtained through pump-probe spectroscopy. The inset shows parabolic energy dispersion for bilayer graphene, where the arrow indicates excitation of electrons from valence to the conduction band. The solid lines represent bi-exponential fits based on the above equation. (b) Tabulated values of relaxation times τ_1 and τ_2, corresponding to intraband carrier-carrier scattering and carrier-phonon scattering, respectively, obtained from the fits.

3. Defects in graphene for energy storage

The increasing global energy demands have spurred a rigorous search for new renewable energy sources. In recent times, fuel cells, photovoltaic devices/solar cells, and various other renewable energy sources have received much attention and are all promising candidates for clean energy production. However, today's batteries and capacitors, which are the main components for energy storage, cannot meet the world's demand for combined power and

energy densities [24–27]. As an example, the plot in **Figure 5** shows the general performance metrics for commercially available formats of charge/energy storage devices. This plot depicts *electrical capacitors* (on the top left hand side) with a fast response time and high-power-density *batteries and fuel cells* (on the bottom right hand side), which exhibit a large energy density due to the chemical/ionic basis of their reactions. The drawback of electrical capacitors is their inability to store large amounts of energy, while the batteries are incapable of fast charge/ discharge cycles due to the slow nature of the ion diffusion processes. This gap between capacitors and battery performance has been a *major roadblock* in electrochemical energy storage. Electrochemical double-layer capacitors (EDLCs) or *supercapacitors* have been proposed to bridge the gap between these disparate devices by incorporating elements of both technologies [12, 28–33]. The charge is stored in the electric double layer, which forms at the electrode/electrolyte interfaces and leads to a double-layer capacitance (C_{dl}). The specific energy (E) of the EDLC may be expressed in terms of the total measured device capacitance (C_{meas}) and the operating voltage (V) as $E = (1/2)C_{meas}V^2$. Unlike traditional Li-ion batteries, EDLCs can be reliably used for hundreds of thousands of cycles since their charge storage mechanism does not involve ion motion and the consequent chemical irreversibility. Although the EDLCs are superior (say, to batteries) in terms of long-term cyclability, they suffer from poor energy density in that energy (or charge) is only stored at the surface/interface rather than within the bulk of the material.
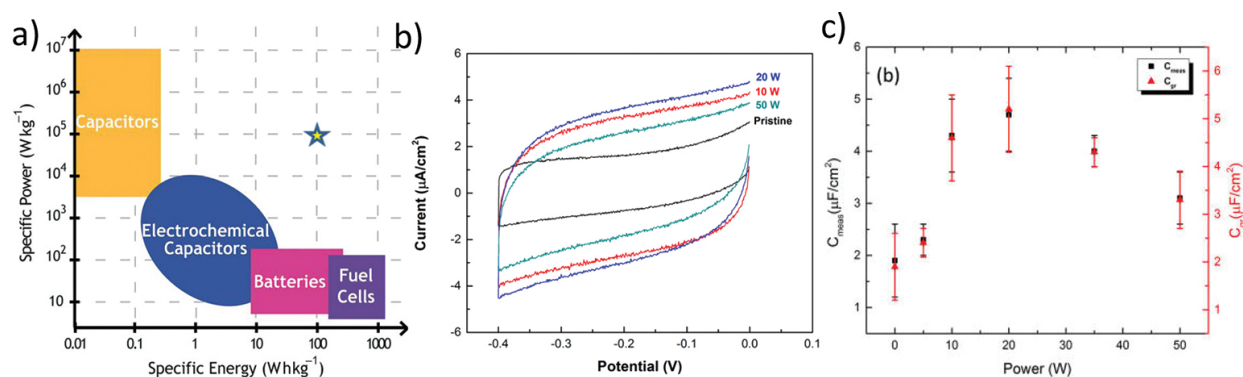
Figure 5. (a) Ragone plot showing specific power versus specific energy for common electrical energy storage devices. Supercapacitors are expected to bridge the gap between batteries and capacitors and impact nearly every area of electrical energy usage. For practical applications, the energy and power densities indicated by the star are needed. (b) Cyclic voltammetry (CV) characterization of plasma processed FLG samples (in 0.25 M TBAHFP dissolved in a 1 M acetonitrile). The area enclosed by the CV curves was used to parametrize the C_{meas} which increases with plasma power (indicated on the figure). (c) A close to threefold enhancement in the C_{meas} (left axis) and the contributions of the computed C_q (right axis), i.e., $1/C_{meas} = 1/C_{dl} + 1/C_q$, as a function of the plasma power.

Nanocarbons including carbon nanotubes and graphene have been widely used as an electrode in EDLCs due to their high surface area (~2000 m^2/g), modest electrical conductivity, electrochemical stability, and open porosity [25, 27]. However, the performance of the carbon-based EDLCs (particularly, graphene) is fundamentally limited by the so-called quantum capacitance (C_q), which is defined as $C_q = e^2DOS(E_F)$ with *e* being the charge of an electron [6]. An intrinsically small DOS (E_F) in graphene results in a small serial C_q, which diminishes the total device

capacitance value ($1/C_{meas} = 1/C_{dl} + 1/C_q$) in EDLCs [6, 28]. Although graphene has high surface area and consequently high C_{dl}, the total EDLC energy is limited by small C_q. Defects can be advantageous for alleviating the limitation of C_q by increasing the DOS (discussed later in **Figures 5b** and **c**). In our previous work [6], we synthesized few-layer graphene (FLG) on Ni foil substrates through chemical vapor deposition and subsequently subjected to argon-based plasma processing to intentionally induce charged defects (see the inset in **Figure 6**). Argon was chosen because the constituent ionic species are limited to Ar+, implying relatively simple plasma chemistry.
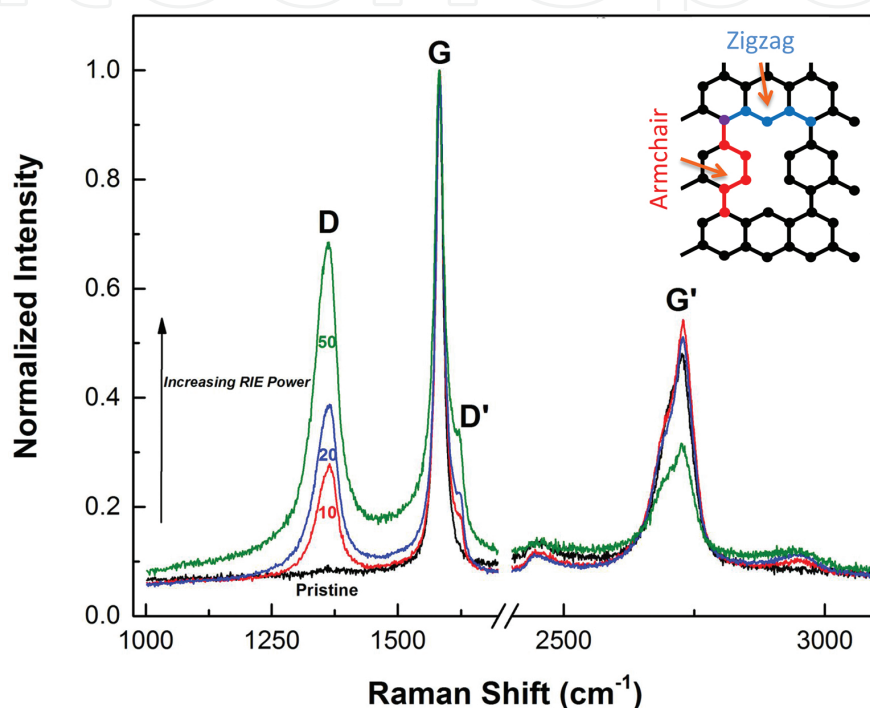
Figure 6. Enhanced plasma processing applied to the pristine sample results in a substantial intensity enhancement of the D- and D′-peaks as seen in the Raman spectra (normalized to the G-peak). An increase in power, say to 50 W, may result in irreversible changes due to graphene removal. The inset schematic shows the difference between armchair and zigzag defects (created using plasma processing) in the graphene lattice.

As shown in **Figure 6**, we found that the D band in the Raman spectrum of graphene increased with increasing power of plasma etching due to the introduction of new structural defects such as pores, which contain both armchair and zigzag edges. An important attribute of zigzag defects is that they may be electrically active and could contribute to an enhanced DOS much more than the armchair-type edge defects (which contribute less due to the two constituent carbon atoms belonging to different sublattices). We observed that the increase in plasma power resulted in a high device capacitance due to higher C_q arising from defect-induced DOS (E_F). Indeed, we used cyclic voltammetry to quantify the changes in C_q and C_{meas} (**Figure 5b**). The more than doubling of the C_{meas} from 1.9 $\mu F/cm^2$ (for the pristine sample) to 4.7 $\mu F/cm^2$ (for the sample subject to 20 W plasma) is remarkable and suggests a novel means of substantially enhancing capacitance through defects. However, at higher plasma power (>20 W), high

defect concentration results in poor electrical conductivity leading to a drop in C_{meas} suggesting the importance of defect concentration in determining 2D material properties.

Thus, as evidenced by our data in graphene, the presence of defects does not necessarily deteriorate the material performance. Though there is only one way for a given material to be defect-free, there are many possibilities for it to be imperfect. While defect configuration is important in determining the mobility through carrier scattering rate, controlling defect concentration is critical for electrochemical applications. Accordingly, future efforts must be focused on finding new approaches to identify and control the right defect configurations (e.g., N in graphitic configuration to increase carrier concentration without compromising carrier scattering rates or mobility) and concentrations, which could improve material properties instead of dismissing all defects as detrimental for carrier mobility.

4. Defects in 2D bulk materials for thermoelectric power generation

Thermoelectric (TE) materials have the potential to reduce global energy crisis and global warming effects by converting waste heat to electricity. As of 2005, the world energy usage was ~15 terawatts of energy, of which ~90 % was first converted to heat and the remainder ~10 % of energy was utilized [24]. In general, power plants and the transportation industry are the two main sources of heat energy losses that contribute to global warming. In recent years, prototype car models developed by automobile industries BMW and Ford have successfully transformed the waste heat from car exhausts to electricity using thermoelectric power generators, thus improving the fuel efficiency [24, 34].

A basic thermoelectric energy conversion module consists of n and p-type semiconducting materials, connected electrically in series and thermally in parallel [35]. The maximum thermoelectric efficiency is a product of the Carnot Efficiency and a term consisting of ZT or the thermoelectric figure of merit, which embodies interrelated material parameters, as given by $ZT = \alpha^2 \sigma T/k$, where α is Seebeck coefficient or thermopower, σ is the electrical conductivity, and $k(= k_E + k_L)$ is the total thermal conductivity comprised of electronic (k_E) and lattice contributions (k_L), respectively. The main challenge of improving the energy conversion efficiency and consequently the ZT of thermoelectric materials is the inherent *coupling* between the electrical conductivity and the Seebeck coefficient. In recent years, there has been significant scientific progress in the field of thermoelectrics with the use of nanostructured materials (e.g., superlattices, nanowires, and nanocomposites) that have simultaneously increased the power factor (the numerator of ZT) and reduced the thermal conductivity to achieve a high $ZT > 1$ [36].

4.1. Quantum confinement effects in 2D thermoelectric materials

In the early 1990s, Hicks et al. [37] predicted intriguing changes in transport properties upon lowering the dimensionality of existing bulk materials (e.g., from 3D to 2D) that were not observed in the corresponding bulk materials. A dramatic increase in the density of states (DOS) of low-dimensional materials was predicted that could increase the Seebeck coefficient

and potentially decouple the electronic transport properties. Moreover, the presence of numerous interfaces in low-dimensional materials also increased phonon scattering effects that reduced the lattice thermal conductivity, thus introducing opportunities to independently vary all the parameters constituting the ZT [38]. In the low-dimensional thermoelectric materials, dramatic changes in the density of states were observed in the PbTe-based thermo-electric materials owing to the quantum confinement effects that led to further *decoupling* of the TE transport properties and an enhancement of ZT [39].

Nevertheless, it is challenging to fabricate low-dimensional materials for commercial thermo-electric applications and devices, which must be a cost-effective and facile process. In addition, the nanostructured thermoelectric materials have to be thermodynamically stable to retain the desired 2D properties over time, to make the devices reliable and long lasting. To be able to make use of the advantages of low-dimensional materials as well as robustness of the bulk materials, bulk nanomaterials or nanocomposites have been used to enhance the thermoelec-tric performance of existing thermoelectric materials such as SiGe and PbTe [40, 41].

Controlling the multi-scale microstructures via defect engineering and consequently the length scales of the electrical and thermal transport is essential for enhancing TE performance. However, material properties (thermopower, electrical, and thermal conductivity) dictating the ultimate compatibility factor and ZT are inherently coupled at the nanoscale. Thus, any efforts to improve only one particular property (e.g., thermopower) using microstructure changes are often futile as they inadvertently deteriorate remaining properties (e.g., electrical conductivity). In this section, we describe how charged defects in 2D materials can introduce low-energy carrier filtering and selective charge carrier scattering (e.g., hole excessively scattered compared to electrons) to improve ZT and compatibility factor in Bi_2Te_3.

4.2. Impact of charged grain boundaries in few-layered Bi_2Te_3

Discovered in the early 1950s by Goldsmid [42], Bi_2Te_3 is one of the most used and commer-cialized TE materials for room-temperature power generation and refrigeration applications [43]. The first TE refrigerator was designed using the *p*-type Bi_2Te_3, which was estimated to have a figure of merit ~ 0.48. In 2001, the thin-film superlattices were reported to exhibit enhanced ZT ~ 2.4 and ~1.4 at 300 K in the *p*-type Bi_2Te_3/Sb_2Te_3 and the *n*-type $Bi_2Te_3/Bi_2Te_{2.83}Se_{0.17}$, respectively [44]. While a high ZT ~ 1.5 was realized in the bulk *p*-type Bi_2Te_3 via nanostructuring techniques such as ball-milling [45], melt-spinning [46, 47], and hydrothermal synthesis [48], it was found that these methods were ineffective for the *n*-type Bi_2Te_3. Like graphite, *n*-type Bi_2Te_3 is easily cleavable, and these traditional nanostructuring methods were too harsh and resulted in the deterioration of its basal plane (or *in-plane*) properties (**Figure 7a**).

Recently, Puneet et al. [5] utilized a novel technique of chemical exfoliation followed by spark plasma sintering (CE-SPS) in the *n*-type $Bi_2Te_{2.7}Se_{0.3}$ that significantly improved the TE compatibility factor and stabilized the ZT peak at higher temperatures (300–450 K) as com-pared to the commercial ingot. Based on the studies of emerging two-dimensional (2D) materials (e.g., graphene), it may be expected that the electronic, thermal, and optical proper-ties of chemically exfoliated *n*-type Bi_2Te_3 should exhibit properties that are different from the

bulk. In the following paragraphs, we discuss the effect of the chemical exfoliation and spark plasma sintering of n-type Bi_2Te_3 as compared to the bulk commercial ingot.

The bulk bismuth telluride (Bi_2Te_3) exhibits a rhombohedral crystal structure belonging to the space group $R\bar{3}m(D5)$, which is more commonly represented by a hexagonal crystal structure as shown in **Figure 7a**. The hexagonal unit cell of Bi_2Te_3 is composed of three quintuples with lattice constants $a = 0.4384$ Å and $c = 3.036$ Å, respectively. As shown in the figure, each quintuple consists of five atoms stacked in the order Te^1-Bi-Te^2-Bi-Te^1 along the c-axis, which are bonded by ionic-covalent bonds. The Te^1-Te^1 layers between the two quintuples are held together by the weak van der Waals forces that make the Bi_2Te_3 easily cleavable. The n-type Bi_2Te_3 was obtained by partially doping Se at the Te^1 or Te^2 sites, which represent the Te atoms with two types of bonding.
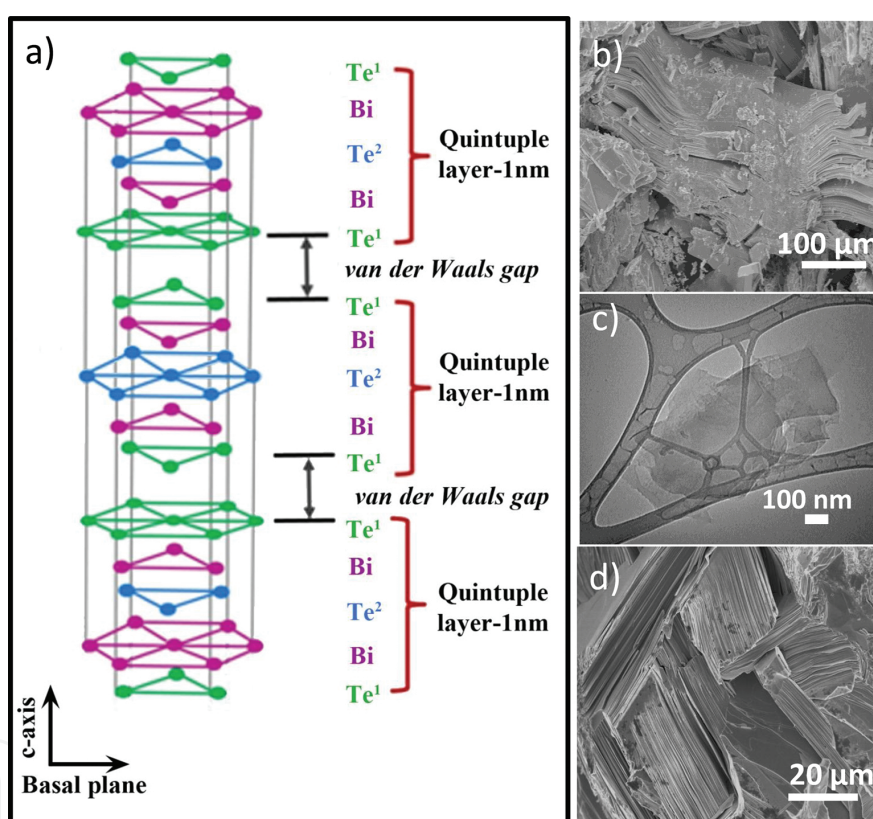

Figure 7. (a) A schematic representation showing Bi_2Te_3 rhombohedral crystal structure belonging to the space group $R\bar{3}m(D5)$. Upon chemical exfoliation, the crystal breaks at the van der Waals gap. (b) A scanning electron micrograph showing the layered structure of bulk Bi_2Te_3 ingot. (c) A transmission electron micrograph showing chemically exfoliated quasi-2D Bi_2Te_3, which is repacked using spark plasma sintering (d) to achieve better thermoelectric performance through charged grain boundaries.

The nanostructuring of the commercial n-type Bi_2Te_3 ingot (see **Figure 7b**, purchased from the Marlow Industries, USA) was achieved by the chemical exfoliation method, using N-methyl-2-pyrrolidone (NMP) solution which was ultrasonicated using a tip sonicator (Branson 250) for 3, 5, 8, or 13 h, respectively. After centrifuging the solution and vacuum filtering the supernatant through a 0.45 mm nylon filter paper, the filtered powder was washed several times using

deionized water to remove any residual NMP. The exfoliated nanolayers (see **Figure 7c**) were ~50 nm in thickness, which were then compacted using the spark plasma sintering (SPS, Dr. Sinter LabH-515S) technique at a holding temperature of 500 °C and an applied pressure of 30 MPa for 5 min under a dynamic vacuum. For the SPS process, the samples were loaded into graphite dies, and the pressure was applied using graphite rods. The resulting SPS-processed pellets were 12.5 mm in diameter and 2–3 mm in thickness, yielding samples with 98–99 % of the theoretical density (see **Figure 7c**).

The rapid densification technique by SPS has distinct advantages over other types of sintering techniques, such as the hot pressing. The SPS process is capable of sintering material powders within a very short time, in the order of minutes [49, 50]. As a result, it is possible to retain the metastable micro-/nanostructures of materials by limiting their grain growth and excessive diffusion during the sintering process. Furthermore, unlike other sintering techniques like hot pressing which uses furnace heating, only the graphite cylinder, rods, and sample are heated by the joule heating produced by pulsed dc in the SPS, which leads to even shorter processing times.
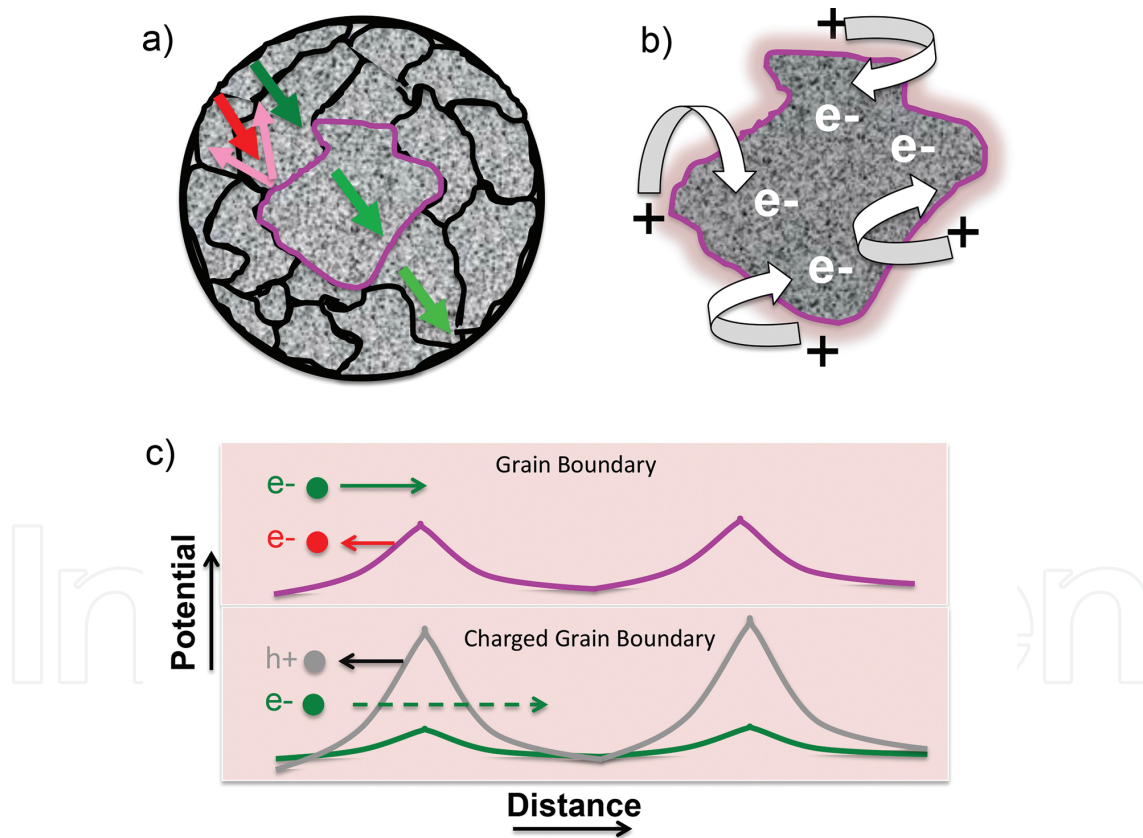
Figure 8. (a) Charged defects near the grain boundaries (GB) can induce excess majority carriers (b) and preferentially scatter holes over electrons and low kinetic energy carriers (red arrow in panels a and c) due to engineered charged GB potential barriers shown in (c).

Contrary to the general understanding that defects in a crystal lattice are detrimental to the transport properties of materials, the defects in 2D materials are extremely useful and could

be manipulated to generate controlled defects for novel and innovative applications. As observed in the few-layered bulk Bi_2Te_3, the localized positive charges in the grain boundaries introduced extra electrons in the material, thereby increasing the carrier concentration n (see **Figure 3a** in Ref. [5]). This increase in n was attributed to the injection of donor-like defects (**Figure 8a** and **b**), arising from positively charged anti-sites/Te vacancies on the exfoliated grain boundaries, due to chemical/mechanical exfoliation [51]. Moreover, these positively charged or interfacial charged *defects* acted as a potential barrier (see **Figure 8c**) to selectively filter out low-energy holes (or minority carriers) as shown schematically by Puneet et al. (see **Figure 3** in Ref. [5]). These charged *defects* in the few-layered n-type Bi_2Te_3 thus shifted the onset of the bipolar (or two carrier) effects and consequently the maximum ZT value to higher temperatures, thus optimizing the ZT over a broader range of temperature. In addition, the thermoelectric compatibility factor of the few-layered n-type Bi_2Te_3 was significantly improved, which determined the ability of these materials to be segmented to other thermoelectric materials such as PbTe at higher temperatures, for operation over a broader range of temperature.

In summary, the CE-SPS processing of 2D Bi_2Te_3 leads to preferential scattering of electrons at charged grain boundaries and optimizes the band filling, thereby increasing the electrical conductivity despite the presence of numerous grain boundaries, and mitigates the bipolar effect via band occupancy optimization leading to an upshift in ZT peak (by ~100 K) and stabilization of the ZT peak over a broad temperature range of ~150 K. These changes in electrical and thermal transport led in turn to a more device-design friendly compatibility factor.

5. Conclusions

As exemplified by graphene and Bi_2Te_3, the presence of defects and dopants imparts the host material with new micro/quantum states or energy configurations that can strongly influence optical, electronic, and thermal properties. In addition to the above properties, S and F dopants are being explored to make graphene magnetic [10, 52–55], while N dopants are expected to provide much higher enhancements in quantum capacitance without compromising electrical conductivity [28]. Similar to Bi_2Te_3, defects in other layered systems such as SnSe and $TaSe_2$ could be engineered to achieve better thermoelectric performance [56–62]. Although this chapter presented only some examples of defects in 2D materials, the same concepts also hold true for other 2D materials such as MoS_2, WS_2, and BN. Indeed, some properties (e.g., luminescence and catalytic activity) of these materials can be tuned using defects [63–68]. As the design and development of new 2D materials are costly, complex, and limited due to the relatively poor air stability of many materials (e.g., silicene and phosphorene), the realization of desired properties and functionalities through control of defects (e.g., vacancies, dopants) in 2D materials is necessary. Though there is only one way for a given material to be defect-free, there are many possibilities for materials to be imperfect. The global scientific endeavors on understanding defects, such as the efforts presented in this chapter, provide a glimpse of the enormous potential of defects warranting further interdisciplinary research efforts.

Author details

Sai Sunil Kumar Mallineni[1], Sriparna Bhattacharya[1], Fengjiao Liu[1], Pooja Puneet[1], Apparao Rao[1,2], Anurag Srivastava[3] and Ramakrishna Podila[1,2,3,4*]

*Address all correspondence to: rpodila@g.clemson.edu

1 Department of Physics and Astronomy, Clemson Nanomaterials Center, Clemson University, Clemson, SC, USA

2 Center for Optical Materials Science and Engineering Technologies, Clemson University, Clemson, SC, USA

3 ABV-Indian Institute of Information Technology and Management, Gwalior, MP, India

4 Laboratory of Nano-bio Physics, Clemson University, Clemson, SC, USA

References

[1] Butler SZ, Hollen SM, Cao L, Cui Y, Gupta JA, Gutiérrez HR, et al. Progress, challenges, and opportunities in two-dimensional materials beyond graphene. ACS Nano. 2013; 7:2898–926.

[2] Geim AK, Novoselov KS. The rise of graphene. Nat Mater [Internet]. 2007;6(3):183–91. Available from: http://www.nature.com/doifinder/10.1038/nmat1849

[3] Bonaccorso F, Sun Z, Hasan T, Ferrari AC. Graphene photonics and optoelectronics. Nat Photonics [Internet]; 2010;4(9):611–22. Available from: http://arxiv.org/abs/1006.4854

[4] Geim a K, Grigorieva I.V. Van der Waals heterostructures. Nature [Internet]; 2013;499(7459):419–25. Available from: http://www.ncbi.nlm.nih.gov/pubmed/23887427

[5] Puneet P, Podila R, Karakaya M, Zhu S, He J, Tritt TM, et al. Preferential scattering by interfacial charged defects for enhanced thermoelectric performance in few-layered n-type Bi_2Te_3. Sci Rep [Internet]. 2013;3:3212. Available from: http://www.pubmedcentral.nih.gov/articlerender.fcgi?artid=3827612&tool=pmcentrez&rendertype=abstract

[6] Narayanan R, Yamada H, Karakaya M, Podila R, Rao AM, Bandaru PR. Modulation of the electrostatic and quantum capacitances of few layered graphenes through plasma processing. Nano Lett.; 2015;15(5):3067–72.

[7] Podila R, Chacón-Torres J, Spear JT, Pichler T, Ayala P, Rao A.M. Spectroscopic investigation of nitrogen doped graphene. Appl Phys Lett [Internet]. 2012;101(12):

123108. Available from: http://link.aip.org/link/APPLAB/v101/i12/p123108/s1&Agg=doi

[8]   Anand B, Karakaya M, Prakash G, Sankara Sai SS, Philip R, Ayala P, et al. Dopant-configuration controlled carrier scattering in graphene. RSC Adv [Internet]; 2015;5(73): 59556–63. Available from: http://xlink.rsc.org/?DOI=C5RA05338B

[9]   Araujo PT, Terrones M, Dresselhaus MS. Defects and impurities in graphene-like materials. Mater. Today. 2012;15:98–109.

[10] Zou X, Yakobson BI. An open canvas—2D materials with defects, disorder, and functionality. Acc Chem Res. 2015;48(1):73–80.

[11] Rao CNR, Gopalakrishnan K, Govindaraj A. Synthesis, properties and applications of graphene doped with boron, nitrogen and other elements. Nano Today. 2014;9: 324–43.

[12] Han J, Zhang LL, Lee S, Oh J, Lee KS, Potts JR, et al. Generation of B-doped graphene nanoplatelets using a solution process and their supercapacitor applications. ACS Nano. 2013;7(1):19–26.

[13] Wei D, Liu Y, Wang Y, Zhang H, Huang L, Yu G. Synthesis of n-doped graphene by chemical vapor deposition and its electrical properties. Nano Lett. 2009;9(5):1752–8.

[14] Park KH, Lee D, Kim J, Song J, Lee YM, Kim HT, et al. Defect-free, size-tunable graphene for high-performance lithium ion battery. Nano Lett. 2014;14(8):4306–13.

[15] Wang M, Jang SK, Jang WJ, Kim M, Park SY, Kim SW, et al. A platform for large-scale graphene electronics - CVD growth of single-layer graphene on CVD-grown hexagonal boron nitride. Adv Mater. 2013;25(19):2746–52.

[16] Paton KR, Varrla E, Backes C, Smith RJ, Khan U, O'Neill A, et al. Scalable production of large quantities of defect-free few-layer graphene by shear exfoliation in liquids. Nat Mater [Internet]. 2014;13(6):624–30. Available from: http://www.ncbi.nlm.nih.gov/pubmed/24747780

[17] Coleman JN. Liquid exfoliation of defect-free graphene. Acc Chem Res. 2013;46(1):14–22.

[18] Lee C, Schibli T. Ultra-short optical pulse generation with single-layer graphene. J Nonlinear Opt Phys Mater [Internet]. 2010;6. Available from: http://arxiv.org/abs/1010.0990\nhttp://www.worldscientific.com/doi/pdf/10.1142/S021886351000573X

[19] Lherbier A, Blase X, Niquet YM, Triozon F, Roche S. Charge transport in chemically doped 2D graphene. Phys Rev Lett. 2008;101(3).

[20] Wang H, Maiyalagan T, Wang X. Review on recent progress in nitrogen-doped graphene: synthesis, characterization, and its potential applications. ACS Catal. 2012;2:781–94.

[21] Susi T, Pichler T, Ayala P. X-ray photoelectron spectroscopy of graphitic carbon nanomaterials doped with heteroatoms. Beilst J Nanotechnol. 2015;6:177–92.

[22] Malard LM, Pimenta MA, Dresselhaus G, Dresselhaus MS. Raman spectroscopy in graphene. Phys Rep. 2009;473:51–87.

[23] Ferrari AC, Meyer JC, Scardaci V, Casiraghi C, Lazzeri M, Mauri F, et al. Raman spectrum of graphene and graphene layers. Phys Rev Lett. 2006;97(18).

[24] Cullen JM, Allwood JM. The efficient use of energy: Tracing the global flow of energy from fuel to service. Energy Policy. 2010;38(1):75–81.

[25] Liu C, Li F, Ma L-P, Cheng H-M. Advanced materials for energy storage. Adv Mater. 2010;22(8):E28–62.

[26] Gogotsi Y. What nano can do for energy storage. ACS Nano. 2014;8:5369–71.

[27] Brownson DAC, Kampouris DK, Banks CE. An overview of graphene in energy production and storage applications. J Power Sources [Internet] . 2011;196(11):4873–85. Available from: http://www.sciencedirect.com/science/article/pii/S0378775311003764

[28] Karakaya M, Zhu J, Raghavendra AJ, Podila R, Parler SG, Kaplan JP, et al. Roll-to-roll production of spray coated N-doped carbon nanotube electrodes for supercapacitors. Appl Phys Lett [Internet]. 2014;105(26):263103. Available from: http://scitation.aip.org/content/aip/journal/apl/105/26/10.1063/1.4905153

[29] Zhou R, Meng C, Zhu F, Li Q, Liu C, Fan S, et al. High-performance supercapacitors using a nanoporous current collector made from super-aligned carbon nanotubes. Nanotechnology. 2010;21(34):345701.

[30] Chen X, Lin H, Chen P, Guan G, Deng J, Peng H. Smart, stretchable supercapacitors. Adv Mater. 2014;26(26):4444–9.

[31] Kim B, Chung H, Kim W. High-performance supercapacitors based on vertically aligned carbon nanotubes and nonaqueous electrolytes. Nanotechnology. 2012;23:155401.

[32] Chen T, Peng H, Durstock M, Dai L. High-performance transparent and stretchable all-solid supercapacitors based on highly aligned carbon nanotube sheets. Sci Rep [Internet]. 2014;4:3612. Available from: http://www.pubmedcentral.nih.gov/articlerender.fcgi?artid=3885879&tool=pmcentrez&rendertype=abstract

[33] Arcila-Velez MR, Zhu J, Childress A, Karakaya M, Podila R, Rao AM, et al. Roll-to-roll synthesis of vertically aligned carbon nanotube electrodes for electrical double layer capacitors. Nano Energy [Internet]. 2014;8:9–16. Available from: http://dx.doi.org/10.1016/j.nanoen.2014.05.004

[34] Karpe S. Thermoelectric power generation using waste heat of automobile. International Journal of Current Engineering and Technology. 2016;4(4):144–8.

[35] Tritt TM. Thermoelectrics run hot and cold. Science (80-) [Internet]. 1996;272(5266): 1276–7. Available from: http://www.sciencemag.org/content/272/5266/1276\nhttp://www.sciencemag.org/content/272/5266/1276.full.pdf\nhttp://www.sciencemag.org/content/272/5266/1276.summary?sid=4cff17c5-fc80-4d5d-9567-95557e8c2b64

[36] Minnich AJ, Dresselhaus MS, Ren ZF, Chen G. Bulk nanostructured thermoelectric materials: current research and future prospects. Energy Environ Sci [Internet]. 2009;2(5):466. Available from: http://xlink.rsc.org/?DOI=b822664b

[37] Hicks LD, Harman TC, Sun X, Dresselhaus MS. Experimental study of the effect of quantum-well structures on the thermoelectric figure of merit. Phys Rev B [Internet]. 1996;53(16):R10493–6. Available from: http://link.aps.org/doi/10.1103/PhysRevB. 53.R10493\nhttp://prb.aps.org/abstract/PRB/v53/i16/pR10493_1\nhttp://prb.aps.org/pdf/PRB/v53/i16/pR10493_1

[38] Dresselhaus MS, Chen G, Tang MY, Yang R, Lee H, Wang D, et al. New directions for low-dimensional thermoelectric materials. Adv Mater. 2007;19(8):1043–53.

[39] Hicks LD, Dresselhaus MS. Effect of quantum-well structures on the thermoelectric figure of merit. Phys Rev B. 1993;47:12727–31. [Internet]. Available from: http://link.aps.org/doi/10.1103/PhysRevB.47.12727

[40] Hsu KF, Loo S, Guo F, Chen W, Dyck JS, Uher C, et al. Cubic AgPb(m)SbTe(2+m): bulk thermoelectric materials with high figure of merit. Science. 2004;303(5659):818–21.

[41] Wang XW, Lee H, Lan YC, Zhu GH, Joshi G, Wang DZ, et al. Enhanced thermoelectric figure of merit in nanostructured n-type silicon germanium bulk alloy. Appl Phys Lett [Internet]. 2008;93(19):193121. Available from: http://scitation.aip.org/content/aip/journal/apl/93/19/10.1063/1.3027060

[42] Goldsmid HJ. Thermoelectric refrigeration. Proc Intersoc Energy Convers Eng Conf. 1964;1:iv, 106.

[43] Goldsmid HJ, Douglas RW. The use of semiconductors in thermoelectric refrigeration. Br J Appl Phys. 2002;5(12):458–458.

[44] Venkatasubramanian R, Siivola E, Colpitts T, O'Quinn B. Thin-film thermoelectric devices with high room-temperature figures of merit. Nature [Internet]. 2001;413(6856): 597–602. Available from: http://www.ncbi.nlm.nih.gov/pubmed/11595940

[45] Poudel B, Hao Q, Ma Y, Lan Y, Minnich A, Yu B, et al. High-thermoelectric performance of nanostructured bismuth antimony telluride bulk alloys. Science. 2008;320(5876):634–8.

[46] Li J-F, Liu W-S, Zhao L-D, Zhou M. High-performance nanostructured thermoelectric materials. NPG Asia Mater. 2010;2(4):152–8.

[47] Xie W, Tang X, Yan Y, Zhang Q, Tritt TM. High thermoelectric performance BiSbTe alloy with unique low-dimensional structure. J Appl Phys. 2009;105(11).

[48] Ji X, He J, Su Z, Gothard N, Tritt TM. Improved thermoelectric performance in poly-crystalline p-type Bi_2Te_3 via an alkali metal salt hydrothermal nanocoating treatment approach. J Appl Phys [Internet]. 2008;104(3):034907. Available from: http://scitation.aip.org/content/aip/journal/jap/104/3/10.1063/1.2963706

[49] Yang K, He J, Su Z, Reppert JB, Skove MJ, Tritt TM, et al. Inter-tube bonding, graphene formation and anisotropic transport properties in spark plasma sintered multi-wall carbon nanotube arrays. Carbon N Y [Internet]. 2010;48(3):756–62. Available from: http://dx.doi.org/10.1016/j.carbon.2009.10.022

[50] Puneet P, Podila R, Zhu S, Skove MJ, Tritt TM, He J, et al. Enhancement of thermoelectric performance of ball-milled bismuth due to spark-plasma-sintering-induced interface modifications. Adv Mater. 2013;25(7):1033–7.

[51] Teweldebrhan D, Goyal V, Balandin AA. Exfoliation and characterization of bismuth telluride atomic quintuples and quasi-two-dimensional crystals. Nano Lett. 2010;10(4): 1209–18.

[52] Yazyev O.V., Helm L. Defect-induced magnetism in graphene. Phys Rev B: Condens Matter Mater Phys. 2007;75(12).

[53] Yazyev O.V. Magnetism in disordered graphene and irradiated graphite. Phys Rev Lett. 2008;101(3).

[54] Sepioni M, Nair RR, Rablen S, Narayanan J, Tuna F, Winpenny R, et al. Limits on intrinsic magnetism in graphene. Phys Rev Lett. 2010;105(20).

[55] Zhu J, Park H, Podila R, Wadehra A, Ayala P, Oliveira L, et al. Magnetic properties of sulfur-doped graphene. J Magn Magn Mater. 2016;401:70–6.

[56] Bovet M, Popović D, Clerc F, Koitzsch C, Probst U, Bucher E, et al. Pseudogapped Fermi surfaces of 1T-TaS2 and 1T-TaSe2: a charge density wave effect. Phys Rev B. 2004;69(12): 1–9.

[57] Demsar J, Forró L, Berger H, Mihailovic D. Femtosecond snapshots of gap-forming charge-density-wave correlations in quasi-two-dimensional dichalcogenides 1T-TaS2 and 2H-TaSe2. Phys Rev B [Internet] . 2002;66(4):041101. Available from: http://arxiv.org/abs/cond-mat/0203590\nhttp://link.aps.org/doi/10.1103/PhysRevB.66.041101

[58] Neal AT, Du Y, Liu H, Ye PD. Two-dimensional TaSe2 metallic crystals: spin-orbit scattering length and breakdown current density. ACS Nano. 2014;8(9):9137–42.

[59] Yan Z, Jiang C, Pope TR, Tsang CF, Stickney JL, Goli P, et al. Phonon and thermal properties of exfoliated TaSe2 thin films. J Appl Phys. 2013;114(20).

[60] Snyder GJ, Toberer ES. Complex thermoelectric materials. Nat Mater. 2008;7(2):105–14.

[61] Wang FQ, Zhang S, Yu J, Wang Q. Thermoelectric properties of single-layered SnSe sheet. Nanoscale [Internet]. 2015;7(38):15962–70. Available from: http://www.ncbi.nlm.nih.gov/pubmed/26367369

[62] Zhao L-D, Lo S-H, Zhang Y, Sun H, Tan G, Uher C, et al. Ultralow thermal conductivity and high thermoelectric figure of merit in SnSe crystals. Nature [Internet]. 2014;508(7496):373–7. Available from: http://www.ncbi.nlm.nih.gov/pubmed/24740068

[63] Kim CJ, Brown L, Graham MW, Hovden R, Havener RW, McEuen PL, et al. Stacking order dependent second harmonic generation and topological defects in h-BN bilayers. Nano Lett. 2013;13(11):5660–5.

[64] Pierret A, Loayza J, Berini B, Betz A, Plaçais B, Ducastelle F, et al. Excitonic recombinations in h-BN: from bulk to exfoliated layers. Phys Rev B: Condens Matter Mater Phys. 2014;89(3).

[65] Yuan S, Roldan R, Katsnelson MI, Guinea F. Effect of point defects on the optical and transport properties of MoS2 and WS2. Phys Rev B: Condens Matter Mater Phys. 2014;90(4).

[66] Chen Z, Forman AJ, Jaramillo TF. Bridging the gap between bulk and nanostructured photoelectrodes: the impact of surface states on the electrocatalytic and photoelectrochemical properties of MoS2. J Phys Chem C. 2013;117(19):9713–22.

[67] Mouri S, Miyauchi Y, Matsuda K. Tunable photoluminescence of monolayer MoS2 via chemical doping. Nano Lett. 2013;13(12):5944–8.

[68] Nan H, Wang Z, Wang W, Liang Z, Lu Y, Chen Q, et al. Strong photoluminescence enhancement of MoS2 through defect engineering and oxygen bonding. ACS Nano. 2014;8(6):5738–45.